2021

Near-Field Propagation Analysis for Vivaldi Antenna Design: Insight Into the Propagation Process for Optimizing the Directivity, Integrity of Signal Transmission, and Efficiency

Ha Hoang
Technological University Dublin, hmanhha@gmail.com

Matthias John
Technological University Dublin, matthias.john@tudublin.ie

Patrick McEvoy
Technological University Dublin, patrick.mcevoy@tudublin.ie

See next page for additional authors

Recommended Citation

H. Hoang, M. John, P. McEvoy and M. J. Ammann, "Near-Field Propagation Analysis for Vivaldi Antenna Design: Insight into the propagation process for optimizing the directivity, integrity of signal transmission, and efficiency," in IEEE Antennas and Propagation Magazine, vol. 63, no. 5, pp. 46-60, Oct. 2021, doi: 10.1109/MAP.2020.3003217.

Funder: Science Foundation Ireland (SFI); European Regional Development Fund

Ha Hoang, Matthias John, Patrick McEvoy, and Max J. Ammann

Near-Field Propagation Analysis for Vivaldi Antenna Design

Insight into the propagation process for optimizing the directivity, integrity of signal transmission, and efficiency.

Refined optimization of complex curve–linear-shaped radiators, such as traveling-wave Vivaldi antennas, can be achieved by considering simulated near fields to interpret in detail the structural influences of a design. The relationships between the space and time distributions of electromagnetic (EM) energy clusters and the geometric features are revealed with appropriate use of impulse response analysis combined with the multiple signal classification (MUSIC) algorithm. This article reports a deeper approach when applied to the adjustment of the geometric features of a traveling-wave antenna based on an analysis of near-field propagation features.

Digital Object Identifier 10.1109/MAP.2020.3003217
Date of current version: 18 August 2020

INTRODUCTION

The Vivaldi antenna was proposed by Gibson [1] in 1979. The natural feature of the Vivaldi tapered slot facilitates the propagation of EM energy in traveling-wave modes to offer a moderately high gain in the endfire direction with a wide bandwidth (BW).

To model EM fields, characterize structural/operational features, and optimize the performances for this type of antenna, various approaches have been implemented.

Transverse EM (TEM)-mode transmission line models have been used to describe the propagating and radiating mechanism of tapered slot antennas. Stepped-width transmission line slots connected end to end were used, and a power continuity criterion solved the effect of the stepped discontinuities in [2], and, in [3], a least-square optimization design process was implemented for input impedance and power division calculation at the junctions of a stepped line by a chain of transmission matrices. However, the model's simplicity limited the accuracy and practical application of such methods.

Improved model accuracy based on approximations to sections of conical slot lines [4], [5] yields E-field distributions and radiating fields from Green's functions. Diffraction effects at the end of the slot and lateral edges were incorporated from a weighting pattern for each edge for better predictions than TEM-mode transmission line models.

While, in general, knowledge of the field propagation of a specific structure is required for modeling, numerical 3D EM solvers segment the radiating structure into a meshed volume of cells with different materials adapted to the geometry. Space, time, or frequency distributions of EM energy in the volume are established, a priori, by solving Maxwell's equations numerically or approximately on a cell-by-cell basis for overall volume while taking account of the excitation and boundary conditions. The EM distribution permits antenna characteristics to be derived, e.g., scattering parameters, far-field response, and so on.

Consecutive improvements in EM wave theory, numerical techniques, fast algorithms, high-performance computing, and material characterization have realized faster, more accurate commercial EM solvers for highly complex, real-life applications [6]. The enhancements have even supported the design of complex antipodal Vivaldi antennas from fractal fern leaf-shaped geometries [7]. By combining EM solvers with feasible design optimization processes, a variety of tapered slot antennas with differing EM responses have been proposed. These are based on optimization of the conventional Vivaldi geometry or on modifications/additions to attain improved performances in [8]–[11]. Explanations of the complex EM characteristics for the Vivaldi geometries and the effects from the added elements in [9]–[11] are based on direct observations of near-field electric (E)/magnetic (H)-field vectors and of metal surface currents.

In this article, an analysis method for the propagation of distributed near fields from a full-wave EM solver for the design of Vivaldi antennas is proposed. With an adequately accurate near-field data set in the time/frequency domains for the antenna geometry with a given excitation, the fields in key sections can be identified and quantified to expose relationships between the antenna geometry and space and/or time/frequency distribution of EM energy. The correlations reveal the effects of geometry on the EM field propagation.

Because the observation of EM energy response on the specific regions of the geometry was implemented based on time-domain impulse response analysis, the analysis result was not be affected by the overlapping of periodic cycles like the conventional frequency-analysis method, and it revealed the propagation progress of the EM energy clusters and the influential parts of the geometry in the workspace. Additionally, EM responses at a consecutive set of points offset along the dominant EM energy flows were observed to analyze the progress of propagation and the scattering components between the sections of the geometry. This avoided subdivisions of the

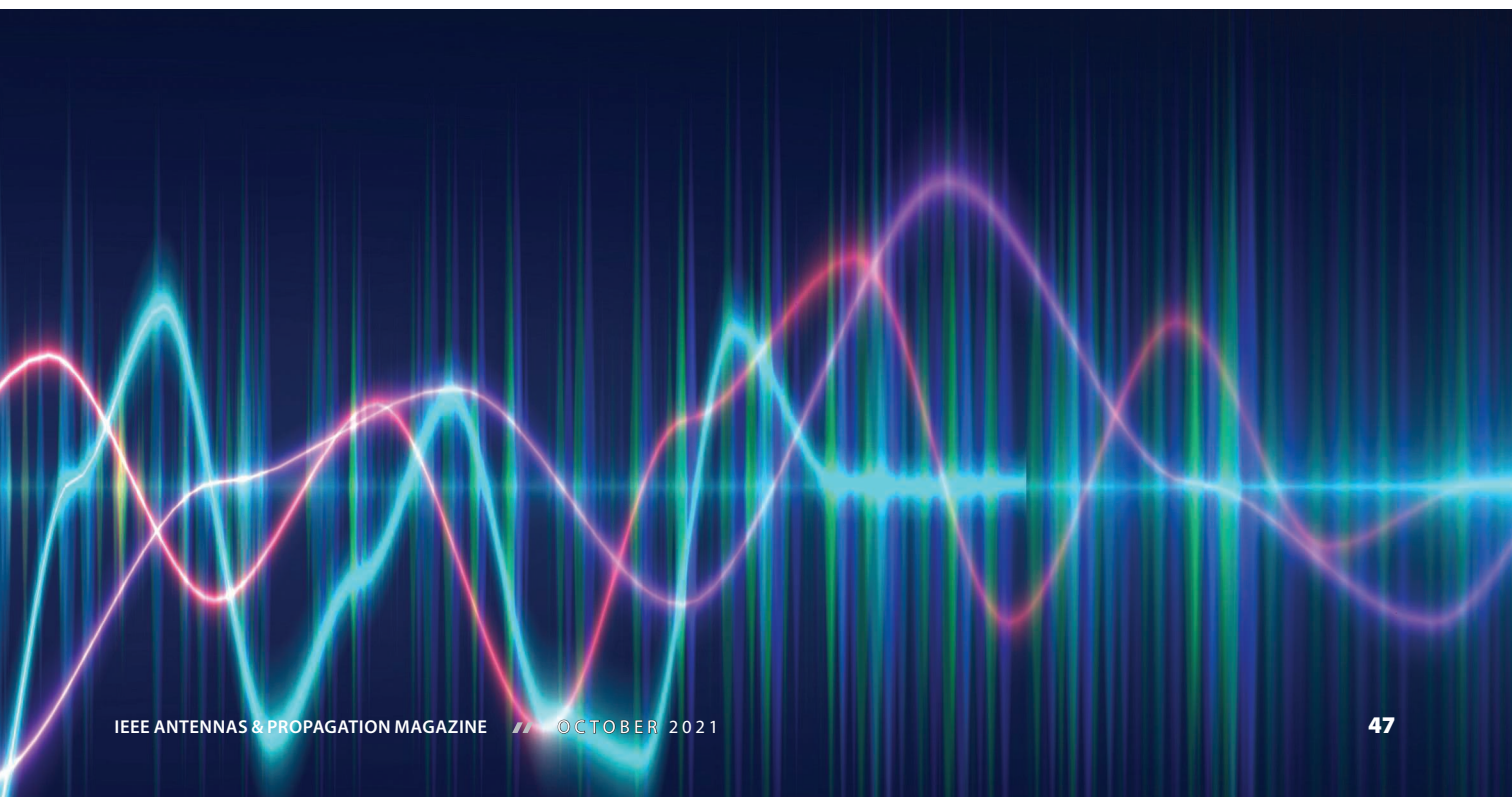

workspace and overcame analysis BW limits. High-resolution analysis using the MUSIC algorithm was also a useful tool.

The rendered detail from space, time, and frequency analyses is a powerful design feature of the method. The quantitative and qualitative analyses examine how the characteristics of a subpart of the time/frequency EM energy response at each point in space and propagation mechanism depend on a particular part of the geometry. Design and optimization methods, built on such analysis, respond for refined adjustment of the structures. The approach reveals a new, deeper perspective in the hierarchy of antenna and related system design.

In this article, an analysis method for the propagation of distributed near fields from a full-wave EM solver for the design of Vivaldi antennas is proposed.

NEAR-FIELD ANALYSIS METHODS

STRUCTURAL DATA, NEAR-FIELD DATA, AND SAMPLING

In this article, CST Microwave Studio (MWS) is used as the EM solver. Structural, meshing, and near-field vector data are extracted for our near-field propagation analysis based on MATLAB. This section presents the features of these data as well as sampling problems and their solutions.

STRUCTURAL AND MESHING DATA

Within the time-domain solver, the hexahedral meshing algorithm is used to generate mesh cells with different material properties to represent the input structure and background space. MWS solves the near-field distribution on this meshed representation rather than the input structure.

Structures like the Vivaldi antenna contain geometric components (Vivaldi curves of the edges) that are not parallel with any of the coordinate axes. This causes a stepped mesh structure to represent these components, as illustrated in Figure 1. Our algorithm extracts the meshing lines and the material matrix data of the whole simulation space and reconstructs the meshed structure.

NEAR-FIELD VECTOR DATA AND SAMPLING

The size and complexity of an EM simulation are governed by the size of the structure and surrounding space, the detail in the structure, and the frequency band of interest. These parameters affect the number of mesh cells and the time step of the EM solver. To achieve high spatial resolution for the analysis, the excitation signal BW must be adequate. It can be larger than the operational BW of the antenna. Additionally, to guarantee convergence, the time step can be much smaller than the time step corresponding to the excitation signal's Nyquist BW; therefore, it does not need to sample all of the computed near-field data. The duration of the EM solver run depends on the length of the excitation signal, volume of the simulation space, degree of EM energy stored in the structure, and accuracy requirement of the analysis, especially for low-frequency or long-delay-time components.

Table 1 presents an example of EM solver parameters for a Vivaldi antenna structure. E-/H-field vectors are sampled in space and time, and each vector is represented by three scalar components, with each component 32 bits (single-precision floating-point format) in size. The total size of the near-field data can reach hundreds of gigabytes.

As the Vivaldi edges are the main structures of the antenna, a significant proportion of EM energy concentrates along them. The space and time distribution of the EM fields on these edges contain most information about the EM energy propagation, and accurate sampling of field data is essential.

The sampling is based on fitting a smooth, nine-order polynomial curve on the step structure of the reconstructed antenna geometry, as shown Figure 1. As expected, this curve represents the Vivaldi edge curve of the input structure, at which there is a transition from metal to dielectric (vacuum) in material properties. Therefore, the field vectors at the edge also have a corresponding transition. To preserve this feature in the

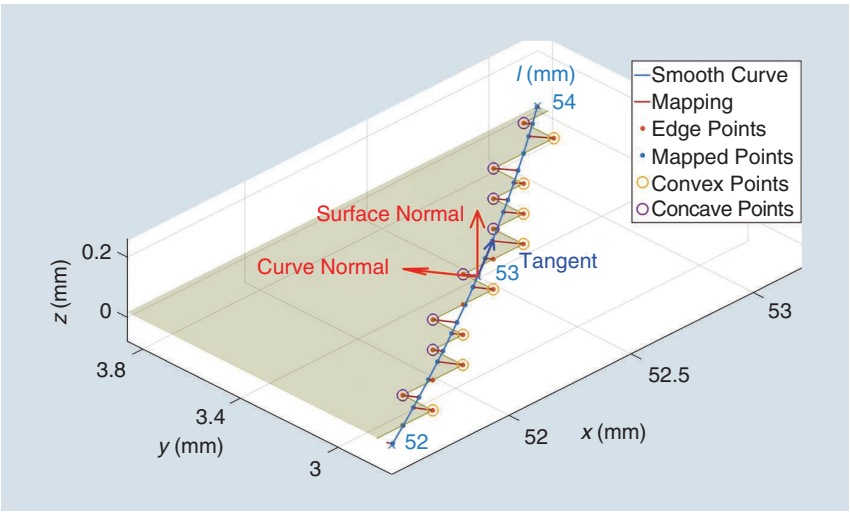

FIGURE 1. The geometrical components and mapping of the Vivaldi edge points to the smooth polynomial curve. Distance *l* is measured from the feed point along the curve edge.

sampled data, the E-H-field vectors at the reconstructed structure edge points are mapped to the nearest points on the smooth curve, and they represent the field on the edge of the input structure. These field vector data can also be divided into tangential and normal vector components, as seen in Figure 1.

The rendered detail from space, time, and frequency analyses is a powerful design feature of the method.

This sampling can also rely on a 3D interpolation of field vector data at mesh cell vertices around the mapped point. However, because the interpolated result depends on the distance to the mapped point and the field vector inside the metallic patch is different from the field vector at the edge of the patch (especially in the vector direction), a significant error can occur in the interpolation result of a mapped point close to a mesh cell vertex inside the metallic patch. The field vector data for the metallic lateral and end edges are collected by extracting the vector data directly on mesh cell vertices corresponding to these edges, and the field vector data for positions in dielectric/vacuum volumes are collected by interpolating data from the nearest mesh cell vertices.

TIME-DOMAIN ANALYSIS METHODS

In the next steps of the analysis, the sampled vector data are derived into scalar/magnitude components. The observed signals can be quantified in different parts in the time/frequency domains. This work focuses on the observation and analysis of the time-domain impulse responses and the utilization of a MUSIC algorithm for time-of-arrival (ToA) estimation of the observed signal clusters.

TIME- AND FREQUENCY-DOMAIN-BASED METHODS

With the time-domain-based method (TDbM), the EM simulation is run with an impulse excitation signal (e.g., Gaussian signal) with a certain analysis BW. The observed signals are extracted directly from the EM solver data. The field responses can be analyzed directly in the time domain or can be converted to the frequency domain using the discrete Fourier transform (DFT).

TABLE 1. AN EXAMPLE OF EM SOLVER PARAMETERS.

Parameters	Values
EM-solving space volume	$84 \times 40 \times 10.267$ mm^3
EM-solving BW	0–81 GHz
Number of mesh cells	11,269,952
Time duration	1.25 ns
Sampling time step	1 ps
Total size of near-field data	320 GB

A disadvantage of this method is that the EM solver must be rerun when the analysis BW changes. To solve this, a frequency-domain-based method (FDbM) is proposed.

With the FDbM, only one EM solver run is necessary, with an excitation signal possessing a large enough BW to cover all analysis band segments. Then, the excitation signal and the observed signals are transformed to the frequency domain by DFT. An equalization is implemented for the frequency components of each observed signal to compensate for the unequal magnitude and phase of the frequency components of the excitation signal.

Inverse DFT is used to transform the compensated observed signals into the time domain. Thus, ideally, if the excitation signal itself is processed, all of its frequency components have the same value in magnitude and phase; when it is transformed to the time domain, it is an impulse signal with full Nyquist BW, and the compensated observed signals are the responses of this impulse. However, the compensation for an observed signal with a certain signal-to-noise ratio (SNR) can gain noise levels excessively for low-energy-level frequency components, especially at the upper end of the band. Therefore, the full Nyquist BW responses cannot be achieved in practice. Limiting the BW for the analysis can be implemented by a window method with the rectangular, Gaussian, and Kaiser windows used in this article. A frequency-modulated continuous wave (FMCW) or linear-chirp waveform is chosen for the excitation signal.

Figure 2 shows an FMCW excitation signal sweeping from 0 to 180 GHz in 0.5 ns and covering a band of 0–210 GHz and impulse signals corresponding to the different windows in the time and frequency domains. Figure 3 shows impulses and responses (the curve normal vector component of the E-field at points along a Vivaldi edge located a distance l from the excitation source) in the time and frequency domains using a Gaussian window in a low-pass analysis band of 0–64 GHz and a bandpass analysis band of 20–90 GHz (–20-dB BW is standard).

An examination of the difference between the TDbM and the FDbM is also implemented. The EM simulation for the TDbM uses a time-domain Gaussian impulse excitation signal with a BW of 0–64 GHz. The EM simulation for the FDbM uses an FMCW excitation signal with a BW of 0–210 GHz, and a Gaussian window with a low-pass BW of 0–64 GHz is applied in the frequency-domain process. Figure 4 shows the impulse signal pair, the response pairs, and their errors. These results demonstrate a good agreement between the two analysis methods.

THE MUSIC ALGORITHM FOR ToA ESTIMATION

MUSIC is a well-known superresolution algorithm used for signal analysis [12], [13]. It is especially powerful in cases of the overlap of many signals and/or limitation in analysis BW. In this article, the MUSIC algorithm is applied for the estimation of ToA(s) or the time delay of a dominant component/cluster of the

observed signals. The excitation signal applied at the antenna port is $x(t)$. Because of multiple overlapping EM energy flows propagating along different paths in the structure, the observed signal at any arbitrary position in the simulation space is a superposition of different versions of the excitation signal. This is considered as a convolution of $x(t)$ and the channel impulse response:

$$s(t) = x(t) \star h(t). \tag{1}$$

In general, $h(t)$ can be continuous, but, in the case of limited excitation signal BW and limits in space/time resolution of the EM simulation, it can be approximated by N discrete components (N can be large):

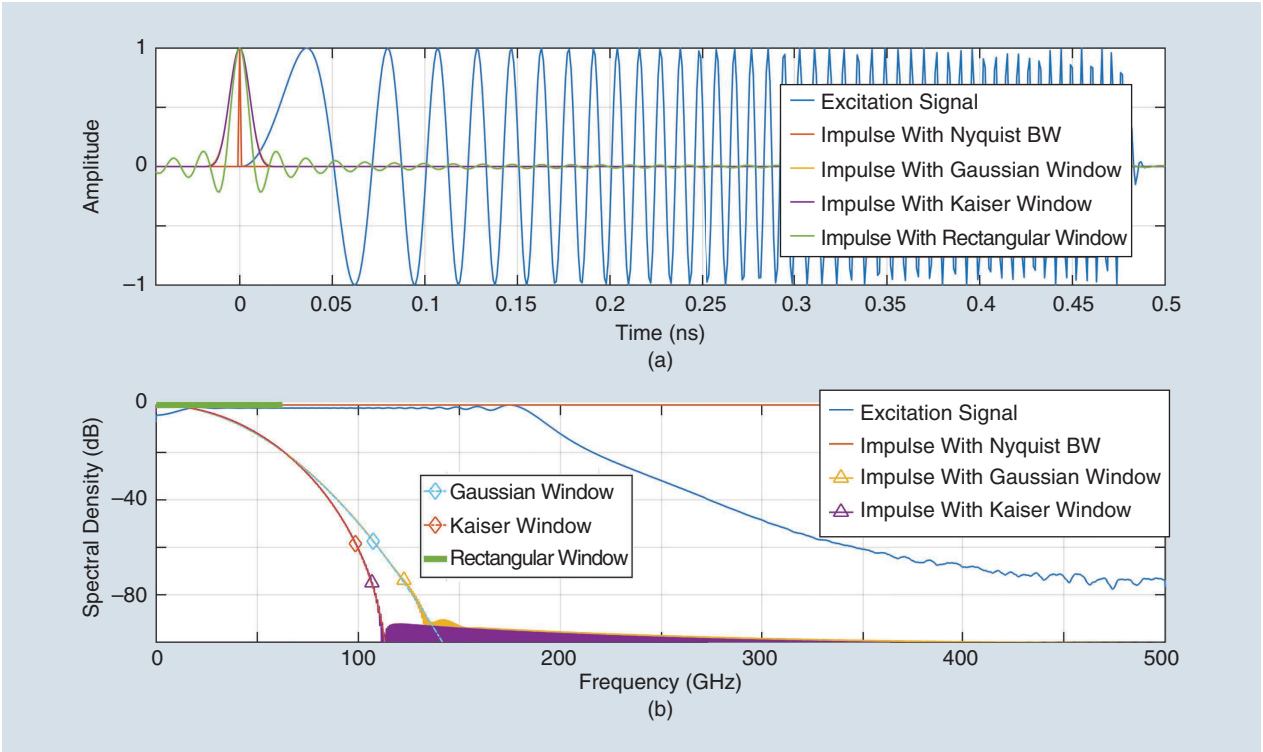

FIGURE 2. The FMCW excitation signal and FDbM impulse signals with different windows in the (a) time and (b) frequency domains.

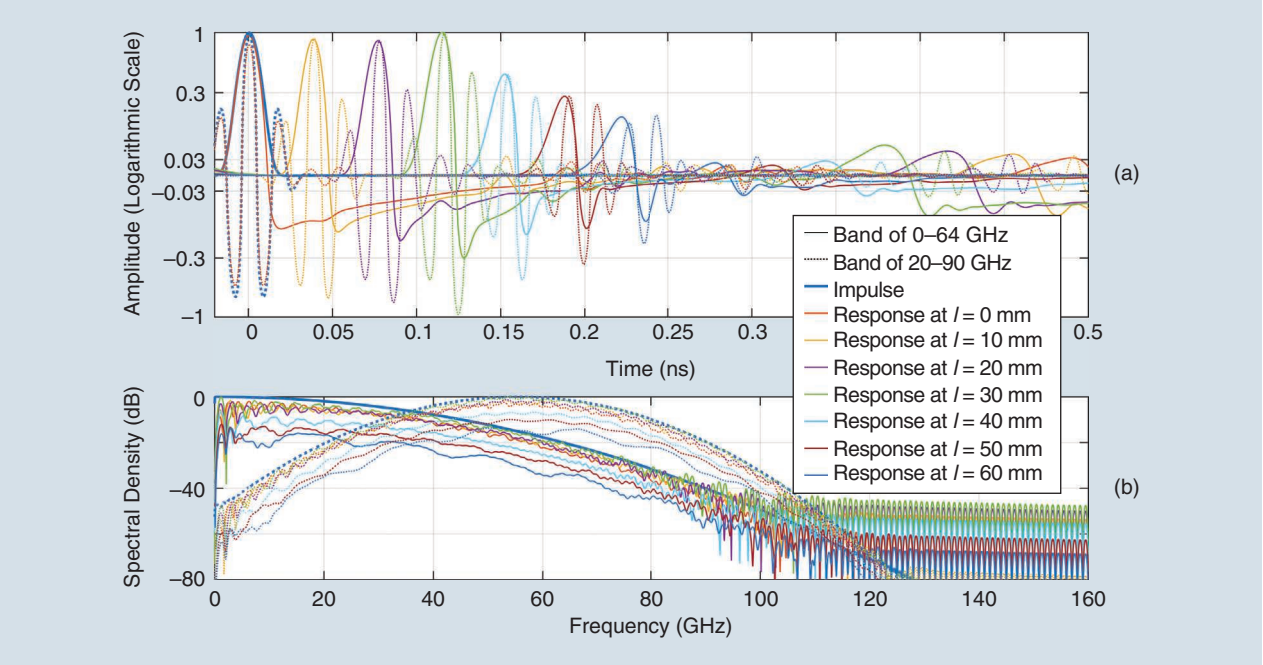

FIGURE 3. The FDbM impulse signal and responses in the (a) time and (b) frequency domains at the points along the Vivaldi edge.

$$h(t) \approx \sum_{n=0}^{N-1} a_n \delta(t - \tau_n), \tag{2}$$

where δ is a Dirac function, and a_n and τ_n are the amplitude and delay time, respectively, of the nth component.

The channel impulse response in the frequency domain is

$$H(f) \approx \sum_{n=0}^{N-1} a_n e^{-j2\pi f \tau_n}. \tag{3}$$

Considering noise (as white noise from EM solver errors) and with a sufficient SNR of the signals in the analysis band, an estimation of $H(f)$ can be implemented as

$$\hat{H}(f) = \frac{\hat{S}(f)}{X(f)} = H(f) + w'(f), \tag{4}$$

where $X(f)$ is the Fourier transform of $x(t)$, $\hat{S}(f)$ is the Fourier transform of $s(t)$ with the noise, and $w'(f)$ is considered as the corresponding white noise in the frequency domain. Then,

$$\hat{H}(f) = \sum_{n=0}^{N-1} a_n e^{-j2\pi f \tau_n} + w(f), \tag{5}$$

where $w(f)$ is the total noise including the error of approximation in (3). $\hat{H}(f)$ in (5) can be considered as a harmonic model [12], [14], and τ_n is the nth parameter needed to be estimated. In this article, the MUSIC algorithm is applied to solve this problem. $\hat{H}(f)$ is sampled in the frequency domain with N_s samples and a frequency step of Δf:

$$\begin{aligned} \hat{H}[k] &= \sum_{n=0}^{N-1} a_n e^{-j2\pi(k\Delta f)\tau_n} + w[k], k = 0, 1, ..., N_s - 1 \\ w[k] &= w(k\Delta f). \end{aligned} \tag{6}$$

The matrix form of $\hat{H}[k]$ is

$$\hat{\mathbf{H}} = \mathbf{V}\mathbf{a} + \mathbf{w}, \tag{7}$$

where

$$\begin{aligned} \hat{\mathbf{H}} &= [\hat{H}[0]\, \hat{H}[1] \ldots \hat{H}[N_s - 1]]^\top \\ \mathbf{V} &= [\mathbf{v}(\tau_0)\, \mathbf{v}(\tau_1) \ldots \mathbf{v}(\tau_{N-1})] \\ \mathbf{v}(\tau_n) &= [1\, e^{-j2\pi((1)\Delta f)\tau_n} \ldots e^{-j2\pi((N_s-1)\Delta f)\tau_n}]^\top \\ \mathbf{a} &= [a_0\, a_1 \ldots a_{N-1}]^\top \\ \mathbf{w} &= [w[0]\, w[1] \ldots w[N_s - 1]]^\top; \end{aligned} \tag{8}$$

$\top$ is a transpose of a vector.

The analysis band limitation is implemented by a rectangular window:

$$\begin{aligned} \hat{H}[k] &= u[k]\left(\sum_{n=0}^{N-1} a_n e^{-j2\pi(k\Delta f)\tau_n} + w[k]\right), \\ k &= 0, 1, \ldots, N_s - 1 \\ u[k] &= \begin{cases} 1 & \text{if } F_{cL} \le k\Delta f \le F_{cH} \\ 0 & \text{otherwise,} \end{cases} \end{aligned} \tag{9}$$

where F_{cL} and F_{cH} are the lower and upper frequency bounds, respectively, of the analysis band.

A Toeplitz data matrix $\mathbf{Z}$ is prepared from $\hat{\mathbf{H}}$ with a dimension factor D chosen as $D \ge N_0$, where $N_0 \le N$ is the size of the signal subspace chosen in the analysis:

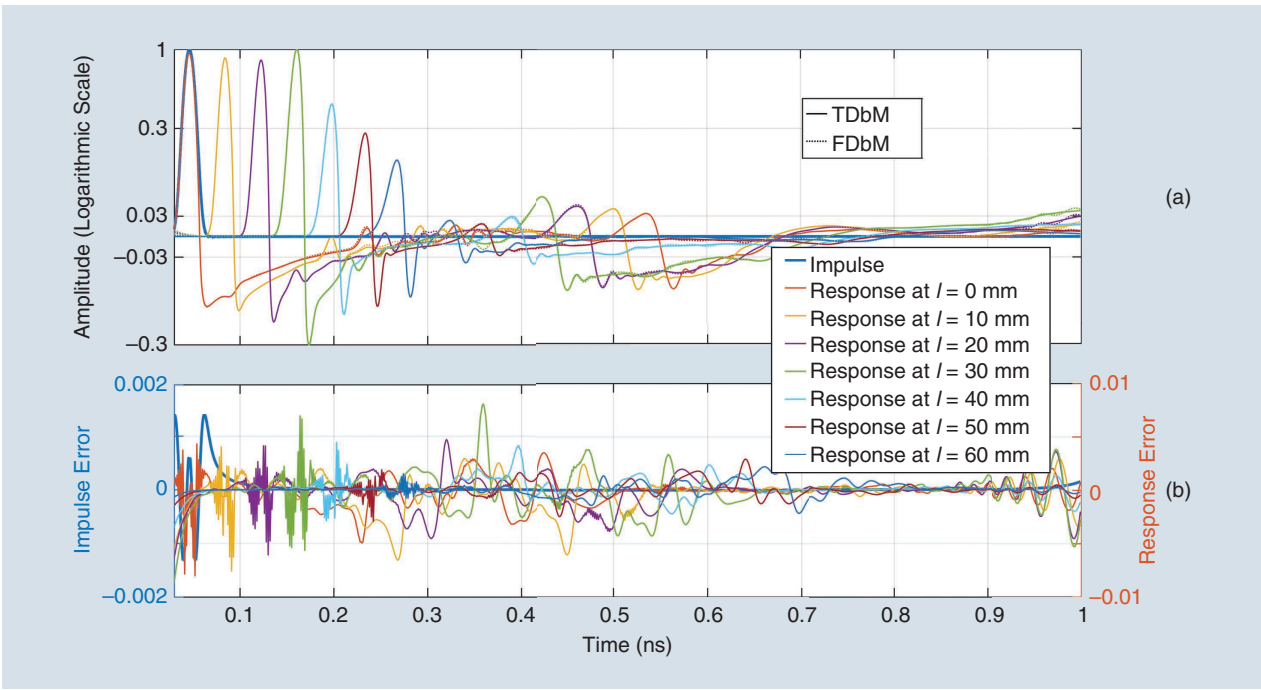

FIGURE 4. The impulse and responses pairs with (a) TDbM and FDbM and (b) the corresponding errors.

$$\mathbf{Z} = \begin{bmatrix} \hat{H}[D] & \cdots & \hat{H}[0] \\ \vdots & \ddots & \vdots \\ \hat{H}[N_s-1-D] & \cdots & \hat{H}[D] \\ \vdots & \ddots & \vdots \\ \hat{H}[N_s-1] & \cdots & \hat{H}[N_s-1-D] \\ \hat{H}^*[0] & \cdots & \hat{H}^*[D] \\ \vdots & \ddots & \vdots \\ \hat{H}^*[D] & \cdots & \hat{H}^*[N_s-1-D] \\ \vdots & \ddots & \vdots \\ \hat{H}^*[N_s-1-D] & \cdots & \hat{H}^*[N_s-1] \end{bmatrix}^{\mathcal{H}}, \quad (10)$$

where $\mathcal{H}$ is a Hermitian transpose of a matrix.

A covariance matrix $\mathbf{R}$ is calculated from the $\mathbf{Z}$ matrix:

$$\mathbf{R} = \mathbf{Z}\mathbf{Z}^{\mathcal{H}}. \quad (11)$$

Eigen decomposition is implemented on the $\mathbf{R}$ matrix, and the signal and noise subspaces are separated [15]:

$$\mathbf{R} = \sum_{i=1}^{D+1} \lambda_i \mathbf{\Psi}_i \mathbf{\Psi}_i^{\mathcal{H}}, \quad (12)$$

where λ_i and $\mathbf{\Psi}_i$ are eigenvalues and eigenvectors, respectively. The ToA parameters can be estimated based on the peak positions of the MUSIC spectrum:

$$P(\tau) = \frac{1}{\left\| \mathbf{\Phi}^{\mathcal{H}} \mathbf{e}(\tau) \right\|^2}, \quad (13)$$

where $\mathbf{\Phi} = [\mathbf{\Psi}_{N_0+1}\, \mathbf{\Psi}_{N_0+2} \ldots \mathbf{\Psi}_{D+1}]$ spans the noise subspace, and $\mathbf{e}(\tau) = [1\ e^{j2\pi\tau/N_s} \ldots e^{j2\pi D\tau/N_s}]^{\top}$ is a steering vector [16].

This MUSIC algorithm is applied to directly analyze the observed signals (curve normal components of the E-field vectors at the points a distance l along an edge of a slot line structure). The analysis is implemented in two cases of $N_0 = 1$ and $N_0 = 500$.

ANALYSIS OF $N_0 = 1$

With $N_0 = 1$, only one component in the signal subspace is expected. It corresponds to the most dominant component/cluster of the observed signal, and others are considered as noise. The peak position of the MUSIC spectrum is expected to indicate the ToA of this dominant component/cluster.

In this analysis, MUSIC parameters are set as $N_0 = 1$; $D = 35$; $N_s = 1,250$; and $dt = 1$ ps, and the analysis is implemented in different bands of F_{cL} and F_{cH}. The FDbM impulse response signals corresponding to the observed signals with the same limiting Gaussian window are calculated as the reference signals.

The estimated ToAs and propagation velocities based on these response signals and the MUSIC spectra are examined and compared, with the results shown in Figures 5 and 6. It is observed in Figure 5 that the FDbM response shape changes with increasing l. The part of the signal to the left of the peak is getting wider than the part to the right of the peak, which tends to increase in negative potential. This is evidence for a left-shifting tendency in the FDbM response peaks versus distance l. Thus, the estimated ToAs based on the FDbM response peaks tends to shrink with distance l. The peak positions of the MUSIC spectra show a regular increase with l.

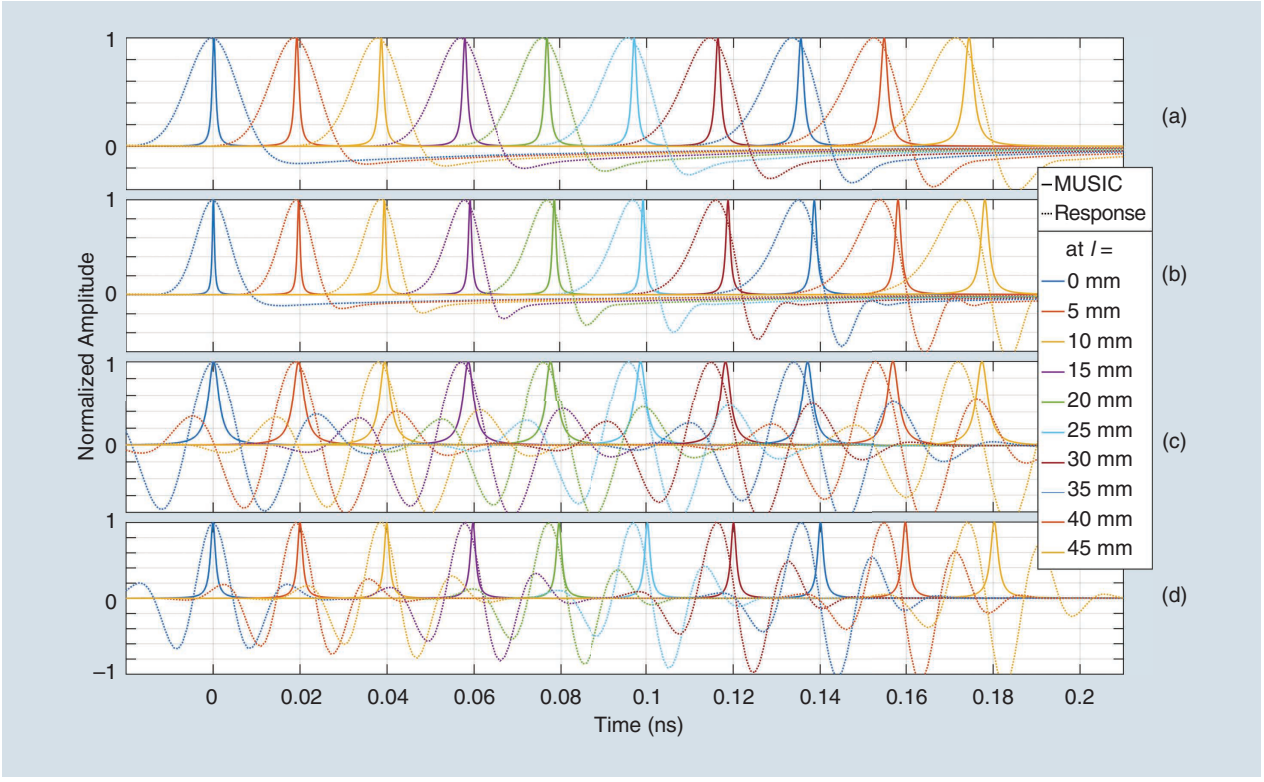

FIGURE 5. The MUSIC spectra and FDbM impulse response signals at the points along the slot line edge with analysis bands of (a) 0–60, (b) 0–90, (c) 20–60, and (d) 20–90 GHz.

This feature can be seen more clearly in the estimated propagation velocities in Figure 6. The estimated velocities based on MUSIC are slower than those based on the response peaks, and the difference increases with an increase in distance l, with the exception of the low-frequency-band case (0–30 GHz), where the two methods show similar results. Additionally, the estimated velocities based on MUSIC show reasonably constant velocities, independent of l, especially in wideband cases.

ANALYSIS OF $N_0 = 500$

This analysis is implemented at a point l = 30 mm on the slot line edge with a selected parameter set of $N_0 = 500$; $D = 738$; $N_s = 1,250$; and $dt = 1$ ps and an analysis band of 0–90 GHz. The dimension factor is chosen as D = 738 to ensure that a full slide over the samples creates a 739 × 1,024 size of the **Z** matrix, and all of its columns contain all of the frequency components of the analysis band without redundancy. This ensures adequate capture of the signal frequency information. FDbM impulse response signals with a Gaussian window and a rectangular window to limit frequency in the same MUSIC analysis band of 0–90 GHz are calculated and shown in Figure 7.

With this analysis of the larger N_0, the MUSIC spectrum is synchronized with the FDbM impulse response signals (with rectangular window); it is also eliminated at nulls of this signal, as seen in Figure 7. This can lead to reduced accuracy in the estimation of the dominant component ToAs that are in proximity to the zero crossings. This effect cannot be observed in the case of $N_0 = 1$. Another feature is that the variability of the magnitude of the MUSIC spectrum peaks is not following the trend of the component/cluster magnitude of the corresponding response. Therefore, the estimation of the component/cluster magnitude needs additional information other than the MUSIC spectrum.

NEAR-FIELD PROPAGATION ANALYSIS

The near-field propagation analysis is implemented on the slot line and Vivaldi structures, as shown in Figure 8. A RT5880 dielectric substrate of width W, length Ls, and thickness h $(-h \le z \le 0)$ is used for the two structures. The metallic

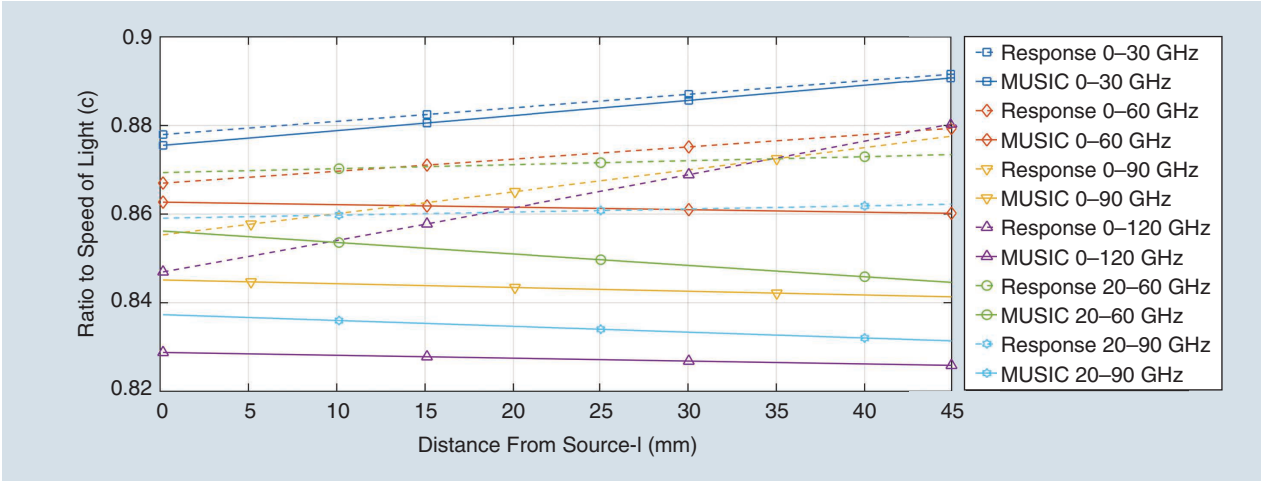

FIGURE 6. The estimated propagation velocities based on the FDbM response signal peaks and the MUSIC spectra in different analysis bands along the slot line edge.

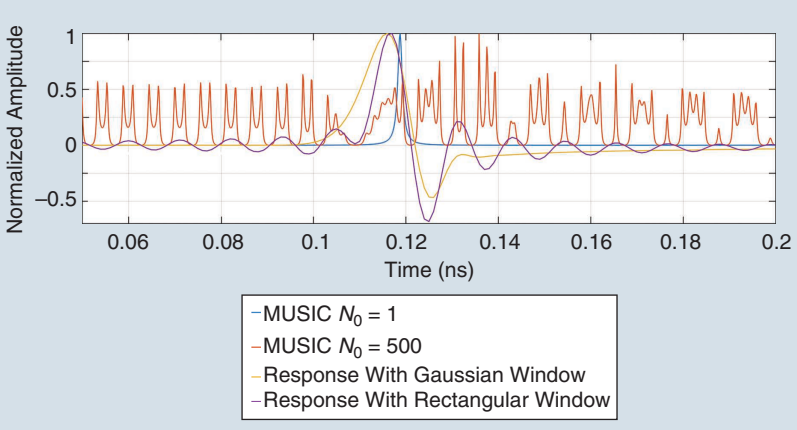

FIGURE 7. The MUSIC spectra and FDbM response signals at a point l = 30 mm along the slot line edge.

objects of the structures are built on the copper layer with a thickness of θ ($0 < z \le \theta$).

The opened-end slot line consists of two copper patches with length L separated by a slot width s. The symmetrical Vivaldi slot is built based on an exponential function (14):

$$y = a(e^{px} - 1) + s/2, \quad 0 \le x \le L, \tag{14}$$

where a is a y-axis scale factor, and

$$a = \frac{(W/2 - s/2) - \varepsilon}{(e^{pL} - 1)}, \tag{15}$$

where ε is the width of the end segment of the Vivaldi element. The x variable and the y curve function are limited to the ranges of $0 \le x \le L$ and $s/2 \le y \le W/2 - \varepsilon$. The parameters of the structures are shown in Table 2.

The time-domain EM simulations were implemented with an open boundary condition with a 5-mm distance from the structures for most of the boundaries, except at the boundary relating to the radiation aperture x_{max}, where the distance is 15 mm. Thus, the volume for the EM simulation is $85 \times 40 \times 10.267$ mm^3. Differential waveguide ports, shown as red squares in Figure 8, with size 4×4 mm^2 ($x = 0, -2$ mm $\le y \le 2$ mm, -2 mm $\le z \le 2$ mm) excite the structures. The excitation signal is an FMCW signal covering a band of 0–210 GHz lasting 0.5 ns. The sampling rate for the observed signals is 1 THz, and the sampled period is 1.25 ns.

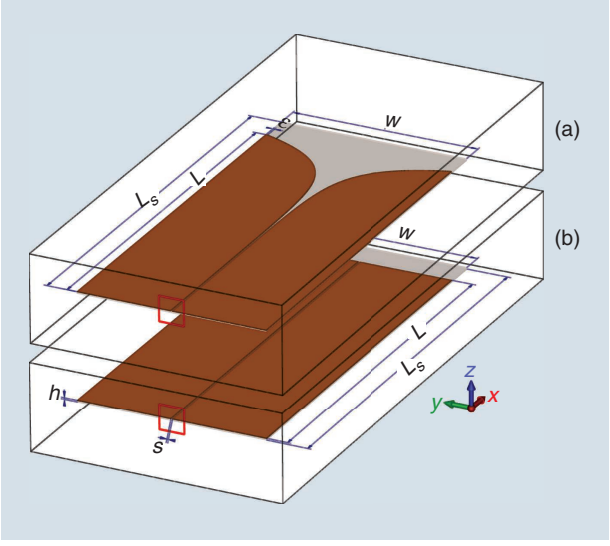

FIGURE 8. The structural models of (a) a Vivaldi antenna and (b) a slot line with excitation ports.

TABLE 2. THE SLOT LINE AND VIVALDI ANTENNA PARAMETERS.

Parameters	Slot Line	Vivaldi Antenna
p	0	0.2
Ls (mm)	65	65
L (mm)	60	60
W (mm)	30	30
s (mm)	0.25	0.25
h (mm)	0.25	0.25
θ (mm)	0.017	0.017
ε (mm)	—	0.25

ANALYSIS OF NEAR-FIELD PROPAGATION ON THE METAL PLANE

The $z = \theta$ plane contains the top surface of the metallic patches and the most valuable field data. The impulse response analysis based on the FDbM with Gaussian windows is implemented for all of the observed signals in this plane in different bands. These complex data are postprocessed, and the results are presented in different forms. In these analyses, the field vector magnitude quantities are normalized according to the maximum magnitude of the corresponding field vectors at the excitation port position ($x = 0, -s/2 \le y \le s/2, z = \theta$).

THE SPACE DISTRIBUTION OF FIELD INTENSITY

This distribution is examined based on the maximum (over time) of the impulse response of E-/H-field vector magnitudes in the two analysis bands. Figure 9 shows these analysis results. Noticeably, the strongest intensities of E-/H-fields distribute along the slot line and Vivaldi slot, especially at the slot metallic edges. In Figure 9(b) and (c), because of the discontinuity in the structure of the meshed Vivaldi slot, as mentioned in the "Structural and Meshing Data" section, at these discontinuous points, there are abrupt changes in the spatial distribution of field intensities. This is an expression of scattering phenomena in the propagation along the tapered structure of the Vivaldi slot.

Other features can be recognized from these plots, e.g., the E-field intensity increases at the endpoints (x = 60 mm) of the slot line and Vivaldi slot, while the H-field intensity reduces at these endpoints. The transition of the dielectric material from RT5880 to vacuum at the substrate edges (60 mm $\le x \le$ 65 mm) in the radiating aperture region can be seen as a discontinuity in the space distribution of the E-field intensity. At the excitation port position, because of the limited port width in the y direction, the H vectors change in direction around the port edge ($x = 0, y = \pm 2$ mm). This leads to the source EM energy being dispersed into multiple directions other than $+x$, as per the definition of the port mode, and these port edges act like scattering sources.

THE SPACE DISTRIBUTION OF THE EARLIEST-ToA CLUSTERS AND MUSIC SPECTRA

The result of the impulse response analysis at each point in space is a time distribution of clusters; this distribution reveals propagating path information (e.g., the number of paths, time delay, and attenuation characteristic). If the time distribution of a certain cluster can be identified for each point in space, then the space-distribution information of this cluster is determined. This information reveals the

effects of the structure's spatial characteristics on the cluster's propagation.

The most important cluster in propagation characterization is the first- or earliest-ToA cluster, which is created by EM energy flows from the source over the shortest transmission path and with the fastest velocity. In this analysis, based on a local peak-finding algorithm, the ToA of the first cluster of the E-/H-field vector magnitudes is estimated for each point in the analysis plane. Information about the direction and magnitude of the field vectors corresponding to the first cluster is derived as shown in Figures 10 and 11. These results reveal how the first cluster vector direction and magnitude are impacted by structure geometric/spatial characteristics. Figure 12 shows the space distribution of propagation times from the source or first-cluster ToAs. With ToA contour lines playing a role as the 2D wavefront, this presents the effects of the geometric/spatial characteristics of the structure on these clusters' propagations visually.

However, due to the limited duration of the analysis impulse and the overlapping of multiple EM currents, the

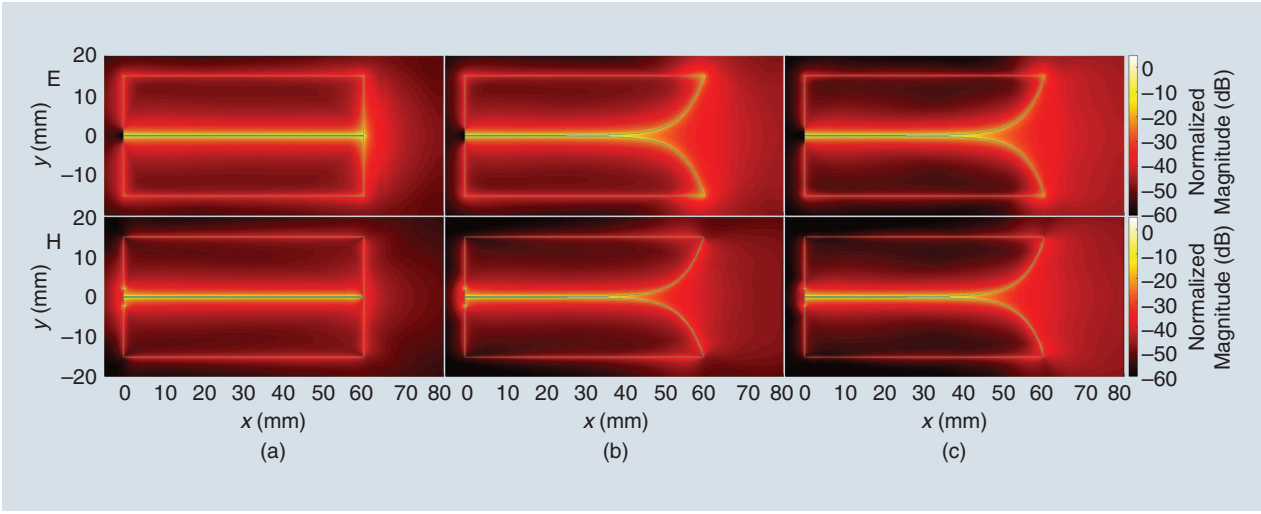

FIGURE 9. The maximum E-/H-field vector magnitudes on the analysis plane $z = \theta$ of (a) a slot line and (b) and (c) a Vivaldi antenna in the analysis bands of (a) and (b) 0–30 and (c) 0–60 GHz.

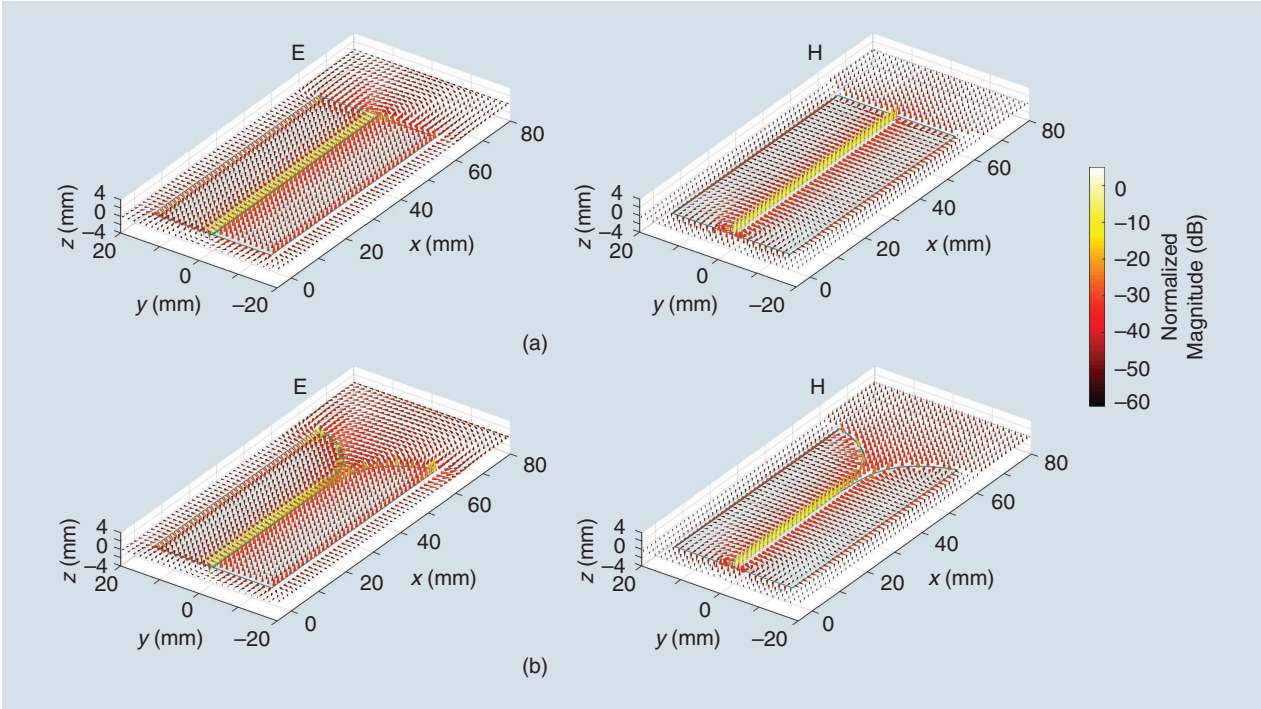

FIGURE 10. The E-/H-field vectors at the time of the first peaks at the selected points on the analysis plane of (a) a slot line and (b) a Vivaldi antenna in the analysis bands of 0–30 GHz.

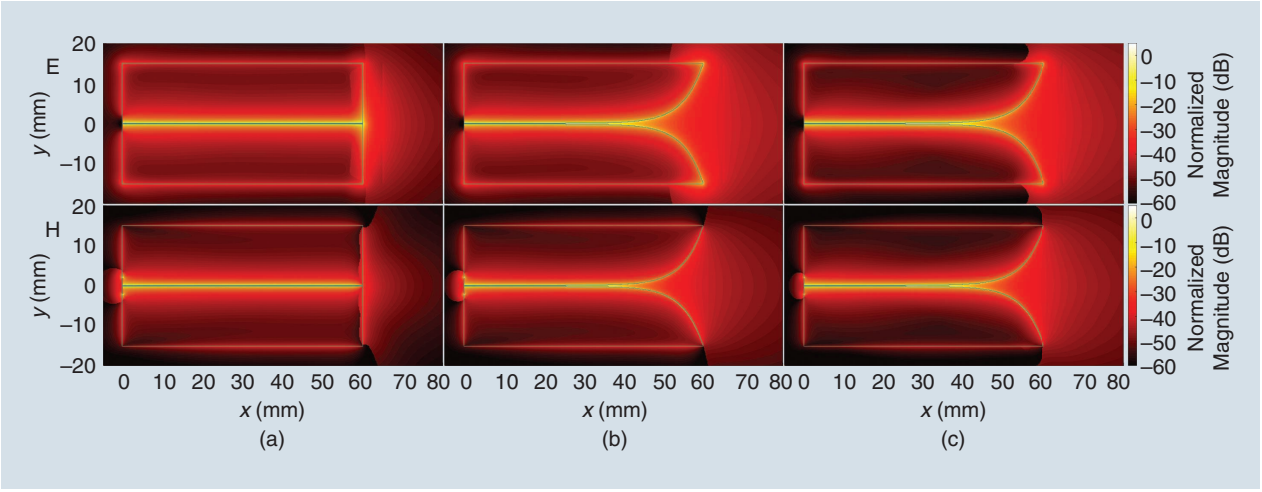

FIGURE 11. The first-peak E-/H-field vector magnitudes on the analysis plane of (a) a slot line and (b) and (c) a Vivaldi antenna in the analysis bands of (a) and (b) 0–30 and (c) 0–60 GHz.

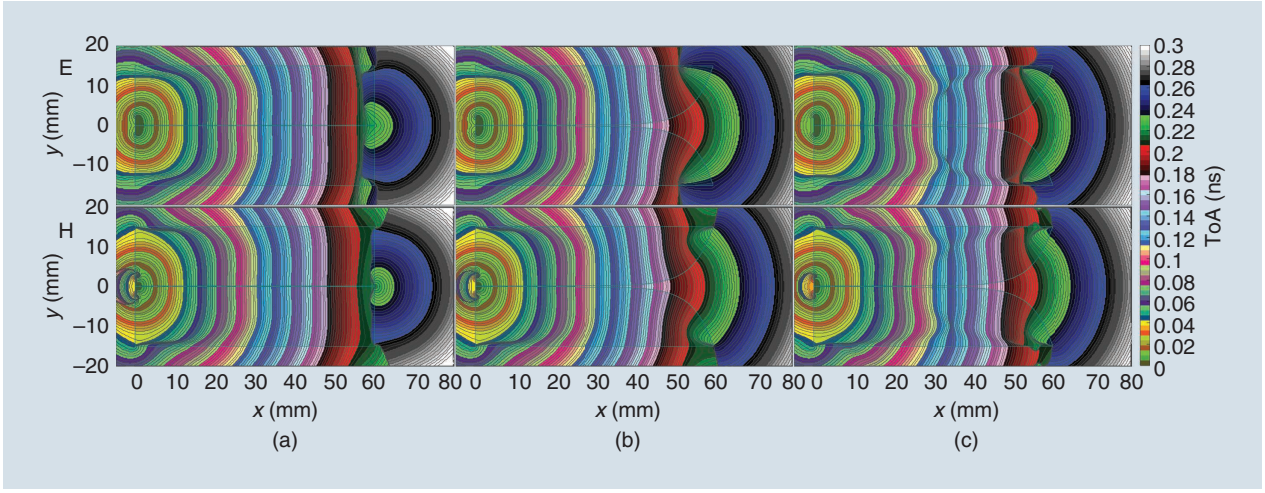

FIGURE 12. The ToAs of the first clusters based on the first peaks of the E-/H-field vector magnitudes on the analysis plane of (a) a slot line and (b) and (c) a Vivaldi antenna in the analysis bands of (a) and (b) 0–30 and (c) 0–60 GHz.

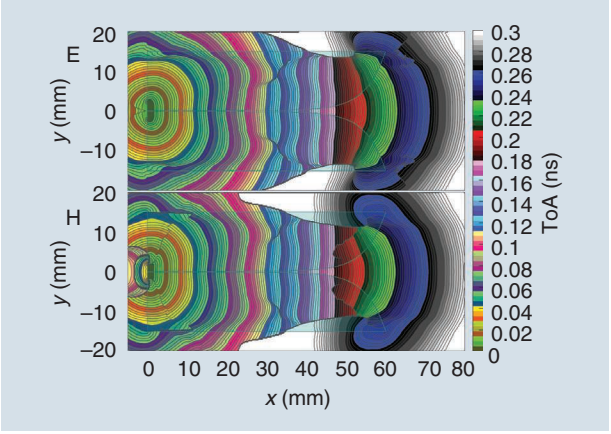

FIGURE 13. The ToAs based on the MUSIC spectra of E-/H-field vectors on the analysis plane of a Vivaldi antenna in the analysis band of 0–60 GHz.

response signals can be flat, cancelled, or not distinguishable as separate clusters. Therefore, time information of the clusters cannot be estimated exactly, or clusters cannot be separated in the time domain, which can lead to significant estimation errors.

The MUSIC algorithm for estimation of the ToA, as mentioned in the "MUSIC Algorithm for ToA Estimation" section is used in this analysis. Figure 13 shows the results of estimated ToAs based on the peaks of the summation of three MUSIC spectrum components of E-/H-field vectors in an analysis band of 0–60 GHz with MUSIC parameters $N_0 = 1$ and $D = 35$. Different from the ToA based on the first cluster of the FDbM responses, these results present ToAs of the dominant components/clusters with a certain correlation with the impulse. In some regions, the MUSIC ToAs are later than the ToAs based on the FDbM response first cluster, as compared in Figures 12(c) and 13.

ANALYSIS OF PROPAGATION ON THE EDGE OF THE SLOTS

In this section, detailed near-field examinations of the slot line and Vivaldi slot metallic edge propagation are made.

FIELD INTENSITY ON THE EDGES

In contrast to the constant distance between the two slot line edges, there are transition positions on the Vivaldi edges of the meshed structure. This leads to abrupt changes in the intensity of the response along the edges, and this is investigated through the first-peak vector magnitudes versus the distance from source l. These magnitudes are normalized according to the first-cluster peak of the corresponding field vector magnitude at the source. The results in Figure 14 show that propagation is similar between the slot line and the Vivaldi slot in the first segment ($0 \le l \le 24$ mm). The transition positions on the edges of the Vivaldi slot lead to scattering at these points, and the magnitudes of both the E and H vectors increase. However, because of this scattering and expansion in slot width after each transition position, the concentration of EM energy flows on the edge in the $+l$ direction after the transition position is reduced. This is demonstrated by faster reduction of the vector magnitudes versus l after each transition position. The overlap between the first cluster and dominant reflecting cluster from the slot-end edge of the slots increases the E vector magnitude and reduces the H vector magnitude.

In contrast to the constant distance between the two slot line edges, there are transition positions on the Vivaldi edges of the meshed structure.

PROPAGATION PROGRESS ALONG THE EDGES

In this section, the response signals at consecutive points along the edges versus time and versus distance l from the source are examined. The effects of the structures on the signals and general propagation progress are analyzed based on the change in cluster shape or emergence of scattering signals versus l. The E-/H-field magnitudes and dominant vector components along the curves are quantities for the analysis. The vector magnitude provides adequate information about the field intensity, while a reversal in vector direction can be observed through the dominant vector components.

To eliminate the difference in intensity at different points on the edges, the signals are normalized according to the first-cluster peaks. Thus, the signal tendencies can be seen clearly with a change of l. The normalized slot line and Vivaldi slot signals against time and l are shown in Figures 15 and 16.

SLOT LINE

Some features of the propagation progress can be recognized from Figure 15 when referring to the magnitudes in Figure 14. Specifically, the A cluster/ledge in Figure 15(a) represents the main cluster transferring from the source through the slot line path in the $+l$ direction. The impulse signal time response of the slot line structure in the propagation progress forms the second cluster (B/B'). In detail, in Figure 15(b), the change in the B cluster signal sign indicates that the vector direction corresponding the B cluster is opposite to that of the A cluster. The reflection of the A (and B) cluster(s) at the slot line open end creates the C cluster propagating in the opposite direction back to the source, and further reflection of the C cluster at the source position creates the E cluster. Some of the A (and B) cluster scattering energy at the slot line open end creates an EM flow traveling along the end edge (x = 60 mm, in the $+y/-y$ direction). This is scattered again at the lateral edge and comes back to the open-end position, creating the D cluster.

VIVALDI SLOT

In addition to the A, B, and C clusters, which are similar to the slot line response, the first-order scattering components on the Vivaldi edge have a significant effect on its propagation progress. Specifically, at the transition positions on the Vivaldi edge, scattering of the A (and B) cluster(s) creates clusters, such as the F and G clusters shown in Figure 16. These transition positions also lead to scattering of the C cluster when traveling in the $-l$ direction. This disperses the C cluster EM energy flow and leads to a reduction in the intensity of the C and E clusters compared to the A cluster (in comparison to the slot line propagation progress). The scattering at the transition positions on the edge and deflection of the Vivaldi curves in the $\pm y$ directions also impact on the A cluster; its width increases, and the peaks are deflected to earlier zones of ToA versus l.

A noticeable feature of the Vivaldi slot propagation is the H cluster. Because of the combination and

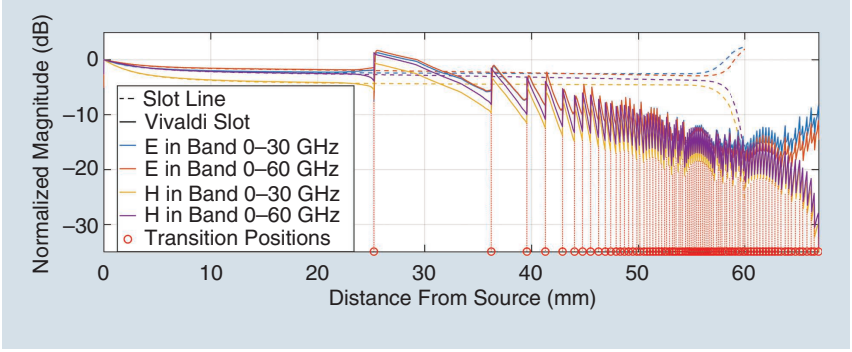

FIGURE 14. The first peak of the E-/H-field vector magnitudes on the edge of the slot line and Vivaldi slot versus the distance from source l.

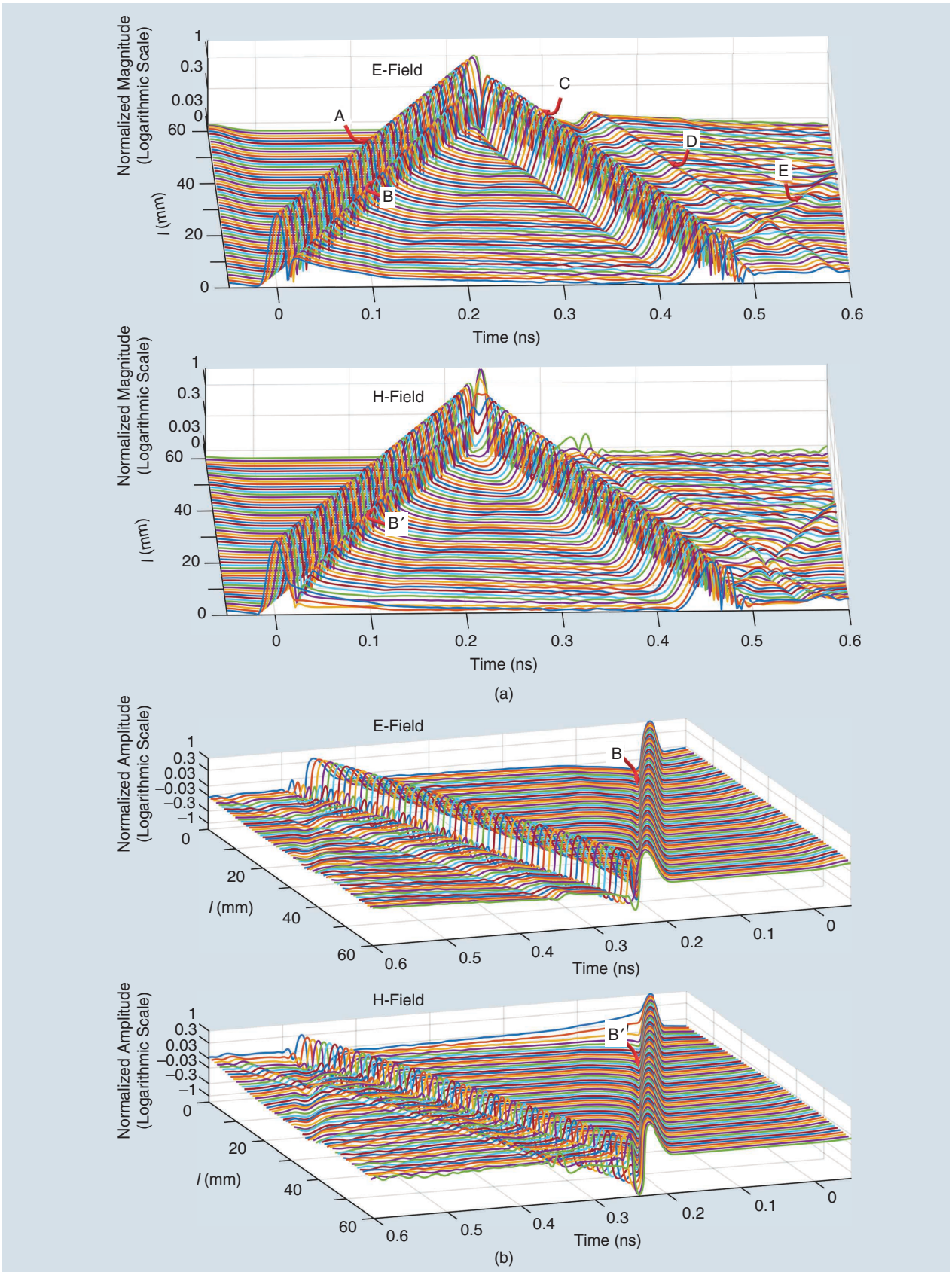

FIGURE 15. (a) The vector magnitude signals and (b) the curve normal/surface normal vector component signals of the E-/H-fields on the edge of the slot line versus time and versus distance from source *l* in the analysis band of 0–60 GHz.

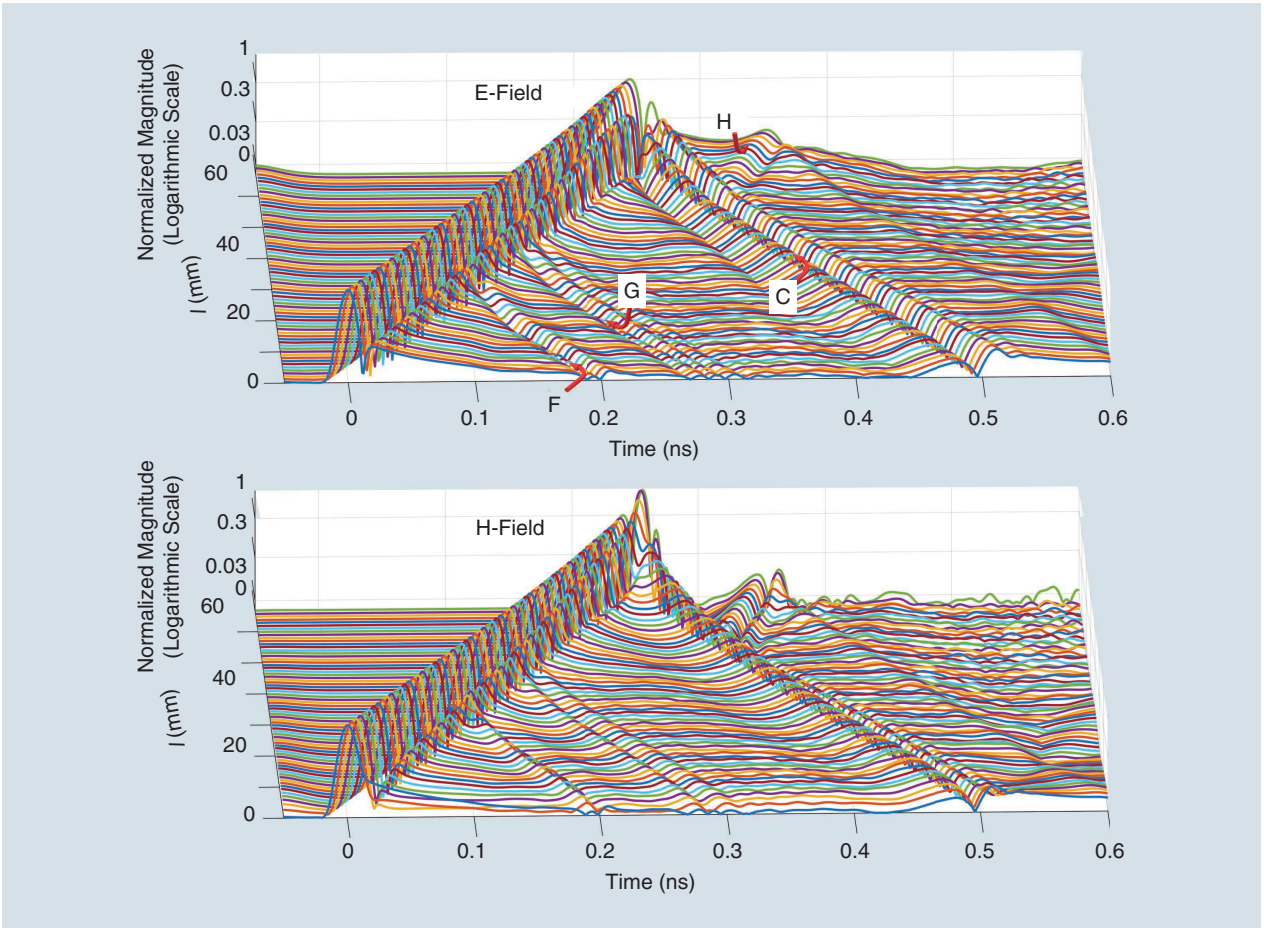

FIGURE 16. The vector magnitude signals of the E-/H-fields on the edge of the Vivaldi slot versus time and versus distance from source *l* in the analysis band of 0–60 GHz.

accumulation of second- and higher-order scattering components arriving from continuous spatial parts, the H cluster is formed. Some examples of paths creating second- and third-order scattering components are illustrated in Figure 17. Assume that point M_1 is the point for time reference of the A cluster, and M_2, having the same position as M_1, is the examined point for the H cluster. A major proportion of the H cluster at M_2 is accumulated from second-order scattering components, such as components propagating over the M_1PM_2, M_1NQM_2, and M_1ORM_2 paths, in which M_1 in the first path; N and O are the first-order scattering points for the A cluster; and P, Q, and R are the second-order scattering points. The intensity of the H cluster is also accumulated from third-order scattering components, such as components traveling in the opposite directions. They travel the M_1QNM_2 and M_1ROM_2 paths, in which M_1 is the first-order scattering point, Q and R are the second-order scattering points, and N and O are the third-order scattering points. Another third-order path is M_1OSOM_2, in which O is the first- and third-order scattering point and S is the second-order scattering point.

DISCUSSION

The plots of the maximum and first-EM-cluster intensity distributions in Figures 9(b) and (c), 10(b), 11(b) and (c), and 14 reveal important regions/points in the Vivaldi structure with high-density EM flow and associated first-order scattering, which contribute to the main EM energy proportion of the total radiation. The scattering degree at the transition points can be assessed primarily by an abrupt change in magnitude by 3–6.5 dB, as seen in Figure 14. The degree of scattering can

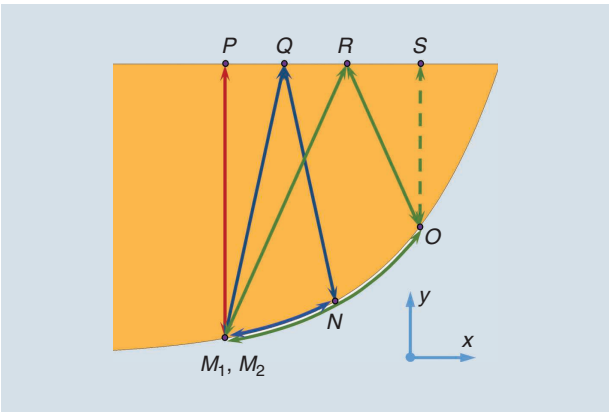

FIGURE 17. Examples of paths of second- and third-order scattering components on the end of the Vivaldi taper.

also be evaluated based on the cluster intensities in Figure 16 with reference to the first-cluster intensities in Figure 14. The reducing magnitude along the Vivaldi curves in Figure 14 indicates the EM energy transfer out of the antenna metal element into the free space.

The flare of the EM flow propagating away from the Vivaldi patches at the antenna aperture, as seen in Figures 10(b), 12(b) and (c), and 13, is a significant factor in the reduction of directivity. Methods to reduce this flare effect are the adjustment of the Vivaldi curve p-factor, addition of a core element, modification of the antenna into a double-slot structure [10], and addition of a material structure at the antenna aperture for adjustment of the directions/velocities of the local EM flows. The estimated results for ToAs, propagating velocities, and EM flow directions (based on the contour curves/surfaces and/or E and H vector directions) at specific regions in the radiating aperture support the effectiveness of the discussed methods.

The formation of H clusters in Figure 16 reveals the higher-order scattering at the lateral edge of the EM flow caused by Vivaldi edge scattering, as illustrated in Figure 17. The scattering on the lateral edge causes partial radiation in unwanted directions and reduces the total directional characteristic. By addition of 45° ripples on the lateral edge [10], part of this energy is redirected into the antenna endfire direction. This improves the antenna gain in a certain frequency band. It also reduces the EM energy portion coming back to the source, thereby improving the S_{11} characteristic.

CONCLUSIONS

This article demonstrates a novel method to reveal, in detail, clusters of EM distributions in space and time and their dependences on particular parts of the structure. This method analyzes the space and time distributions of simulated near-field data based on the impulse response analysis combined with the MUSIC algorithm and considers structural data along with effects due to meshing. These insights into propagating and radiating processes of the near field to the structural shapes can inform the design of wideband traveling-wave antennas to achieve optimization in the efficiency, propagation direction, gain performance, and integrity of signal transmission.

ACKNOWLEDGMENTS

This work was supported, in part, by the Science Foundation Ireland and was cofunded by the European Regional Development Fund under grant 13/RC/2077.

AUTHOR INFORMATION

Ha Hoang (hmanhha@gmail.com) is a Ph.D. student in the Antenna and High-Frequency Research Centre at Technological University Dublin, Ireland, and a lecturer at Ho Chi Minh City University of Technology, Vietnam. His research interests include antenna and microwave circuit design, ultrawideband radar/imaging systems, and electromagnetic simulation and analysis. He is a Member of IEEE.

Matthias John (matthias.john@tudublin.ie) is a senior researcher in the Antenna and High-Frequency Research Centre at Technological University Dublin, Ireland. His research interests include antenna miniaturization and device integration, efficient numerical optimization techniques, radio-frequency identification, radar, and imaging applications. He is a Senior Member of IEEE.

Patrick McEvoy (patrick.mcevoy@tudublin.ie) is a senior researcher and lecturer in the Antenna and High-Frequency Research Centre at Technological University Dublin, Ireland. He is a Senior Member of IEEE.

Max J. Ammann (max.ammann@tudublin.ie) is a professor at Technological University Dublin, Ireland, where he is the director of the Antenna and High-Frequency Research Centre. He is a Fellow of IEEE.

REFERENCES

[1] P. J. Gibson, "The Vivaldi aerial," in *Proc. 9th European Microwave Conf.*, Brighton, U.K., Sept. 1979, pp. 101–105. doi: 10.1109/EUMA.1979.332681.

[2] R. Janaswamy and D. Schaubert, "Analysis of the tapered slot antenna," *IEEE Trans. Antennas Propag.*, vol. 35, no. 9, pp. 1058–1065, 1987. doi: 10.1109/TAP.1987.1144218.

[3] H. Oraizi and S. Jam, "Optimum design of tapered slot antenna profile," *IEEE Trans. Antennas Propag.*, vol. 51, no. 8, pp. 1987–1995, 2003. doi: 10.1109/TAP.2003.811090.

[4] B. Stockbroeckx and A. Vander Vorst, "Electromagnetic modes in conical transmission lines with application to the linearly tapered slot antenna," *IEEE Trans. Antennas Propag.*, vol. 48, no. 3, pp. 447–455, 2000. doi: 10.1109/8.841906.

[5] B. Stockbroeckx and A. Vander Vorst, "Copolar and cross-polar radiation of Vivaldi antenna on dielectric substrate," *IEEE Trans. Antennas Propag.*, vol. 48, no. 1, pp. 19–25, 2000. doi: 10.1109/8.827381.

[6] O. Ergul and L. Gurel, *The Multilevel Fast Multipole Algorithm (MLFMA) for Solving Large-Scale Computational Electromagnetics Problems*. Hoboken, NJ: Wiley, 2014, p. 2.

[7] B. Biswas, R. Ghatak, and D. R. Poddar, "A fern fractal leaf inspired wideband antipodal Vivaldi antenna for microwave imaging system," *IEEE Trans. Antennas Propag.*, vol. 65, no. 11, pp. 6126–6129, 2017. doi: 10.1109/TAP.2017.2748361.

[8] J. Bai, S. Shi, and D. W. Prather, "Modified compact antipodal Vivaldi antenna for 4–50-GHz UWB application," *IEEE Trans. Microw. Theory Techn.*, vol. 59, no. 4, pp. 1051–1057, 2011. doi: 10.1109/TMTT.2011.2113970.

[9] M. Abbak, M. N. Akinci, M. Çayören, and İ. Akduman, "Experimental microwave imaging with a novel corrugated Vivaldi antenna," *IEEE Trans. Antennas Propag.*, vol. 65, no. 6, pp. 3302–3307, 2017. doi: 10.1109/TAP.2017.2670228.

[10] H. Hoang, K. Yang, M. John, P. McEvoy, and M. J. Ammann, "Ka-band planar Vivaldi antenna with a core for high gain," *IET Microw., Antennas Propag.*, vol. 13, no. 6, pp. 732–735, 2019. doi: 10.1049/iet-map.2018.5834.

[11] I. T. Nassar and T. M. Weller, "A novel method for improving antipodal Vivaldi antenna performance," *IEEE Trans. Antennas Propag.*, vol. 63, no. 7, pp. 3321–3324, 2015. doi: 10.1109/TAP.2015.2429749.

[12] N. Alsindi, X. Li, and K. Pahlavan, "Analysis of time of arrival estimation using wideband measurements of indoor radio propagations," *IEEE Trans. Instrum. Meas.*, vol. 56, no. 5, pp. 1537–1545, 2007. doi: 10.1109/TIM.2007.904481.

[13] E. D. Di Claudio, R. Parisi, and G. Jacovitti, "Space time MUSIC: Consistent signal subspace estimation for wideband sensor arrays," *IEEE Trans. Signal Process.*, vol. 66, no. 10, pp. 2685–2699, 2018. doi: 10.1109/TSP.2018.2811746.

[14] D. G. Manolakis, V. K. Ingle, and S. M. Kogon, *Statistical and Adaptive Signal Processing*. New York: McGraw-Hill, 2000, pp. 149–445, 478.

[15] F. Fereidoony, M. A. Sebt, S. Chamaani, and S. A. Mirtaheri, "Model-based super-resolution time-delay estimation with sample rate consideration," *IET Signal Process.*, vol. 10, no. 4, pp. 376–384, 2016. doi: 10.1049/iet-spr.2015.0378.

[16] F.-X. Ge, D. Shen, Y. Peng, and V. O. K. Li, "Super-resolution time delay estimation in multipath environments," *IEEE Trans. Circuits Syst. I, Reg. Papers*, vol. 54, no. 9, pp. 1977–1986, 2007. doi: 10.1109/TCSI.2007.904693.